Centrifugally spun TiO_2/C composite fibers prepared from TiS_2/PAN precursor fibers as binder-free anodes for LIBS

Jorge Lopez [a], Ramiro Gonzalez [a], Jonathan Ayala [a], Jesus Cantu [b], Alexandria Castillo [b], Jason Parsons [b], Jason Myers [c], Timothy P. Lodge [d], Mataz Alcoutlabi [a,*]

[a] Department of Mechanical Engineering University of Texas, Rio Grande Valley, 1201 W University Dr, Edinburg, TX, 78539, USA
[b] Department of Chemistry University of Texas, Rio Grande Valley, 1 W University Blvd, Brownsville, TX, 78521, USA
[c] College of Science and Engineering, 55 Shepherd Labs, University of Minnesota, Minnesota, 55455-0431, USA
[d] Department of Chemical Engineering and Materials Science and Department of Chemistry, University of Minnesota, Minneapolis, MN, 55455-0431, USA

ARTICLE INFO

ABSTRACT

TiO_2/carbon composite-fiber anodes for lithium ion batteries were prepared through the centrifugal spinning of TiS_2/polyacrylonitrile (PAN) precursor fibers and subsequent thermal treatment. The TiS_2/PAN precursor solutions were prepared by mixing TiS_2 nanoparticles (a 2-D layered structure) with PAN in N, N-dimethylformamide (DMF). The thermal treatment of the TiS_2 in the centrifugally spun PAN fibers resulted in TiO_2/carbon composite fibers. The structure of TiO_2 nanoparticles embedded in the carbon-fiber matrix synthesized from the TiS_2 starting material may accommodate high amounts of Li ions. The TiO_2/C structure may lead to increased specific capacity, improved stability, and enhanced electrochemical performance of the TiO_2/C composite electrode after prolonged charge/discharge cycles. The TiO_2/C composite-fiber anode delivered discharge and charge capacities at the first cycle of 683 mAhg^{-1} and 356 mAhg^{-1}, respectively, with a reversible charge capacity of 290 mAhg^{-1} after 100 cycles at a current density of 100 mAg^{-1}. The TiO_2/C composite fibers showed an improvement in the rate performance at higher current densities compared to the graphite anode alone.

1. Introduction

Lithium-ion batteries (LIBs) have been extensively used to power electronic devices as well as electrical vehicles due to their light weight, high energy density, and specific power [1,2]. Recently, research efforts have focused to improve the relatively low performance of rechargeable lithium-ion batteries at high discharge/charge rates. The ability for high discharge/charge rates is vital for the implementation of LIBs in the market for portable energy storage devices. Graphite as an anode material has been the only commercially available material for rechargeable LIBs, due to its low cost and good cycle stability. However, graphite anodes have a relatively low theoretical capacity of 372 mAhg^{-1} [3–5]. The low theoretical capacity limits the potential to meet the increasing demands of advanced energy storage systems, especially in high power applications. Therefore, it has become imperative to design anode materials with improved safety, high capacity, and good rate capability for potential applications in electronics and electrical vehicles.

Recently, silicon (Si) and tin (Sn)-based materials have attracted much attention as potential high-capacity anodes for lithium-ion batteries (LIBs). However, the main drawback to Si and Sn based materials is the high-volume change encountered after prolonged charge/discharge cycles. High volume changes can result in capacity fading, anode cracking, and electrode pulverization [6,7]. Several methods have been used to reduce the volume change and increase the conductivity of Si- and Sn-based anodes including, but not limited to, the synthesis and design of nanostructured anode materials comprising Si and/or Sn nanostructures (e.g., nanoparticles, nanorods, nanospheres) embedded the nanoparticles in a carbon matrix (carbon nanofibers, nanotubes, graphene). Research in the Si/C and Sn/C nanocomposites as potential anodes for LIBs has been focused due to the buffering effect and high conductivity of the carbon matrix [4,8,9]. Transition metal sulfides or transition metal dichalcogenides (TMDC) are also promising anode materials for LIBs owing to their high theoretical capacities, low cost, and ease of availability [4,10]. Certain TMDCs have a 2D morphology consisting of stacked layers with empty space between the layers, which can host a large amount of Li$^+$, and result in a high

---

* Corresponding author.
  E-mail address: mataz.alcoutlabi@utrgv.edu (M. Alcoutlabi).

theoretical capacity for the anode [10]. However, capacity fading, low conductivity, and poor cycle performance are drawbacks to their potential applications [4,11]. Among these TMDCs are molybdenum (Mo), tungsten (W), and titanium (Ti) chalcogens (sulfur (S), selenium (Se) or tellurium (Te) in group IV). The TMDC can act as a host network that can intercalate compounds or atoms. The intercalation results in stored atoms/ions or molecules between the host layered structure causing an expansion of the crystal along the c-axis [12]. Transition metal sulfides including but not limited to, MoS2, SnS2, ZrS2, and TiS2 have a layered structure that allows for more lithium intercalation via a conversion reaction mechanism resulting in the formation of metal nanoparticles and Li2S during the first discharge process (lithiation) in LIBs [13–15]. However, TMDC-based anodes exhibit a high irreversible capacity in the first cycle during the de-alloying process (delithiation), which is caused by the fact that Li-ions cannot be easily extracted from the Li-sulfide alloy [11,15].

To overcome the high irreversible capacity, graphene/TMDC nanocomposites and TMDC composite nanofibers have been prepared to improve the conductivity and electrochemical performance of TMDC-based anodes [15–18]. Titanium disulfide (TiS$_2$) is a TMDC that has been used as both cathode and anode materials in LIBs [19–22]. TiS$_2$ anode has been used in LIBs due to its light weight, low cost, low volume change after a prolonged alloying/de-alloying process, and long cycle life [19]. However, TiS$_2$-based anodes suffer from a high irreversible capacity at the first cycle and safety-related issues caused by dendrite formation in liquid electrolytes preventing commercial use in rechargeable LIBs. Furthermore, TiS$_2$ is also known for its high discharge voltage plateau of 2.1 V versus Li/Li$^+$ and has been mainly used as cathode material in LIBs [19,23,24]. TiS$_2$ has also been investigated as an insertion anode for sodium (Na) and zinc (Zn) ion batteries [24–26].

Metal sulfide/oxide/C composite fibers have already produced through electrospinning and subsequent thermal treatment for use as anode materials in LIBs. The carbon-fiber matrix in these composites can accommodate the high-volume change associated with the metal sulfide and oxides after alloying/de-alloying. The accommodation of the volume change can result in better cycle performance of the anode. Improvement in the electrochemical performance of the composite-fibers anodes can be attributed to the high surface area of the nanofibers, short diffusion pathways for both Li-ions and electrons, abundant active sites for Li storage, as well as higher structural stability of the electrodes [4,27,28]. In addition, the mixed metal sulfide/oxide/C composite electrodes using titanium have high charge/discharge potential of TiO$_2$ (1.7–1.5 V vs Li/Li$^+$), which can suppress the Li-dendrite formation observed in the graphite anode at low delithiation potential (0.1 V vs Li/Li$^+$). Results reported on 2D TiO$_2$-based anode materials such as nanoflakes, nanosheets, and anatase petal-like TiO$_2$ nanosheets have shown that 2D-TiO$_2$ electrodes deliver higher capacity and good cycling stability due to the exposed facets, shortened paths, and preserved porous structures [29,30]. TiO$_2$, nanofibers, nanotubes, nanorods, and nanowires have been also investigated as potential anodes for LIBs. The TiO$_2$ in the anatase phase with a 2D-sheet like structure has been synthesized using TiS$_2$ as a starting material [31]. To the authors' knowledge, results have not been reported on 2-D TiO$_2$ nanoparticles with layered structures used with carbon fibers as composite electrodes for LIBs [27,32,33].

In the present work, TiO$_2$/C composite fibers were prepared from centrifugally spun TiS$_2$/PAN precursor fibers, followed by stabilization in air and calcination in an argon atmosphere. The prepared composite fibers were characterized using a combination of SEM, TEM, XRD, EDAX and XPS. The morphology and structure of the TiO$_2$/C composite fibers show that the TiS$_2$ nanoparticles are converted into 2-D sheet layered titanium dioxide (TiO$_2$) nanoparticles after the oxidation and calcination processes. In addition, the electrochemical performance of the TiO$_2$/C composite anode in Li-ion half cells was systematically investigated.

2. Experimental

2.1. Preparation of TiS$_2$ precursor

Titanium (IV) sulfide (TiS$_2$) was synthesized using a method described by Prabakar et al. [34]. In brief, 120 mmol of elemental sulfur was added to 250 mL of 1-octadecene (Fisher Scientific). The reaction flask was continually purged with argon gas and heated to 300 °C. Once the reaction mixture reached 300 °C, 20 mmol of titanium tetrachloride (Fisher Scientific) was injected. The reaction mixture was refluxed for 30 min at the desired temperature of 300 °C. Subsequent to reflux, the reaction cooled to room temperature naturally. A black precipitate was produced, which was filtered and washed using a combination of methanol, toluene, and acetone to remove the any residual organic solvent and any byproducts that may have formed during the reaction.

2.2. Preparation of TiO$_2$/Carbon composite fibers

Polyacrylonitrile (PAN) ($M_\mathrm{w} = 130,000$) was purchased from Sigma Aldrich (USA), while solvent N,N-dimethyl formamide (DMF) was obtained from Fisher Scientific (USA). The TiO$_2$/C composite fibers were prepared by centrifugal spinning (Cyclone L-1000 M, FibeRio Technology) of a TiS$_2$/PAN precursor solution followed by stabilization of the precursor fibers in air at 280 °C for 5 h and then by calcination at 800 °C for 2 h in an argon atmosphere (heat rate of 2 °C/min). The Force-spinning® process has been described previously [35,36]. The precursor solution was prepared by dissolving PAN in DMF solvent containing the TiS$_2$ nanoparticles. The solution was first sonicated for 30 min to produce a homogenous solution before adding the polymer. The weight ratio of TiS$_2$ to PAN in the solution was adjusted to 2:8 (i.e. 20 wt%). PAN was then added to the solution and stirred for 48 h at room temperature to obtain a homogenous TiS$_2$/PAN solution. The solution was prepared from 88 wt% DMF and 12 wt% of (polymer and TiS$_2$). The TiS$_2$/PAN precursor fibers were then prepared by centrifugal spinning by injecting 1.5 mL of the precursor solution into the spinneret. The quality of fibers was dependent on the solution viscosity, rotational speed of the spinneret, as well as the surrounding temperature and humidity. To obtain fiber diameters in the nano to micro range, the spinneret rotational speed, the spinning time as well as the viscosity of the solution (i.e. concentration) were optimized and set at 7000 rpm, 90 s and 12 wt%, respectively. The fibers were suspended on the collectors after each 2–5 min run of the cyclone; the fibers were transferred on a 10×10 cm^2 metal collector after each run. Fibrous mats of TiS$_2$/PAN were collected with a desired thickness and were then dried in a vacuum oven for 24 h at 100 °C.

2.3. Characterization

The morphology of the TiS$_2$/PAN and TiO$_2$/C composite fibers was characterized by scanning electron microscopy (SEM) using a Sigma VP Carl Zeiss instrument, coupled with an energy dispersive spectroscopy (EDS) system (EDAX, Mahwah, NJ, USA) to investigate the elemental composition of the fibers. Transmission electron microscopy (TEM) images and selected area electron diffraction (SAED) images were recorded using a FEI G2 F30 microscope operated at 300 kV. High-angle annular dark field (HAADF) scanning TEM (STEM) and EDS maps were collected with a FEI G2 Titan 60–300 probe corrected microscope equipped with a Super-X EDS system. The Titan was operated at 200 kV with a convergence angle of 24 mrad and HAADF inner collection angle of 58.5 mrad. X-ray photoelectron spectrometry (XPS) was conducted using a Thermoscientific K-α instrument equipped with monochromatized Al Kα radiation (1486.7 eV). For all the XPS tests, a spot size of 400 μm for the X-ray beam was implemented. The crystal structure of the composite fibers and TiS$_2$ nanoparticles was characterized by X-ray diffraction (XRD), where the patterns were collected from 2θ = 10–90° with a step of 0.1° using a Rigaku Miniflex II X-ray
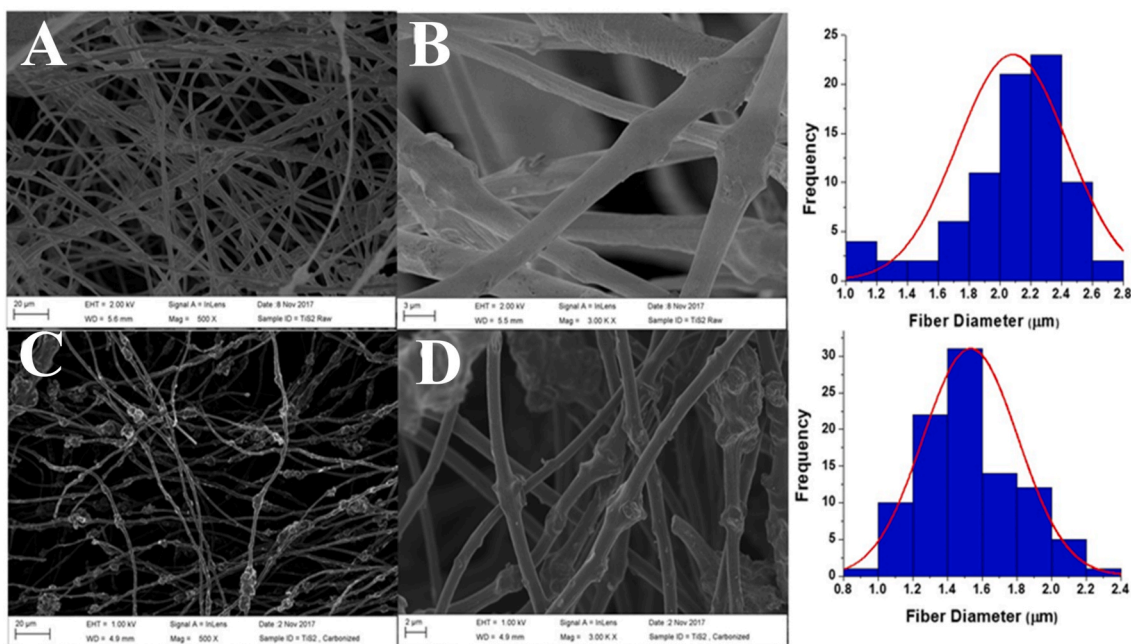
Fig. 1. SEM images at different magnifications of TiS_2/PAN composite fibers (a and b) and carbonized TiO_2/C composite fibers (c and d).

Diffractometer equipped with a copper source (K_α λ = 1.54 Å).

Thermogravimetric analysis (PerkinElmer, Model TGA-7) was performed using a ramping/heating rate of 10 °C/min in air atmosphere. Differential scanning calorimetry (DSC) Model: DSC 214 Polyma, Netzsch (Germany) with a heating rate of 5 °C/min in nitrogen atmosphere.

2.4. Electrochemical performance evaluation

2032 coin-type cells (PHD Energy Inc.) were used to evaluate the electrochemical performance of the TiO_2/C composite-fiber anodes. The electrodes were cut into 2-inch discs and used directly as free standing and working electrodes in the Li-half cells. Lithium metal was used as the counter electrode and glass microfibers were used as the separator. The electrolyte was a 1 M $LiPF_6$ salt in ethylene carbonate (EC)/dimethyl carbonate (DMC) (1:1 v/v) solvent. The Li-half cells were assembled in

an argon-filled glove box (O_2, H_2O concentrations < 0.5 ppm MBraun, USA). The galvanostatic discharge (Li-insertion) and charge (Li-deinsertion) experiments were performed using Li-half cells at different current densities and a LANHE Battery Testing System (CT2001A) over a voltage range of 0.01–3.00 V vs. Li/Li^+ at room temperature. The cyclic voltammetry experiments were conducted using an Arbin automatic battery cycler at a scan rate of 0.1 mV s^{-1} and a range between 0.05 and 2.80 V to investigate the lithium insertion kinetics into the host TiO_2/C composite fibers. Electrochemical impedance spectroscopy measurements were carried out over the frequency range from 1 kHz to 0.005 Hz using Autolab PGSTAT 128 N, Metrohm.

3. Results and discussion

Fig. 1 shows the SEM images of the TiS_2/PAN composite fibers before and after carbonization. The TiS_2/PAN precursor fibers were continuous
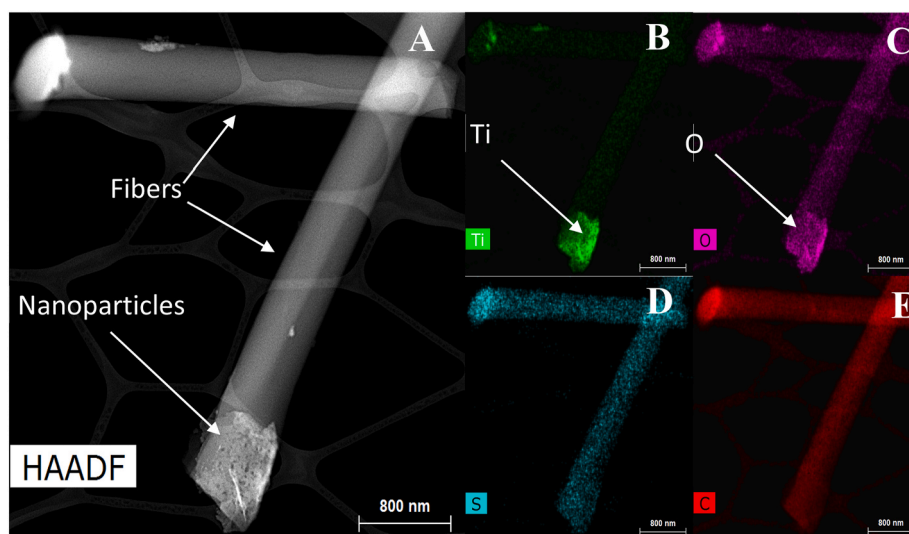

Fig. 2. High-angle annular dark-field (HAADF)-STEM and EDS elemental maps for carbonized TiO_2/C composite fibers, A) TEM image of TiO_2/C fibers; (B–E) elemental mapping for titanium, oxygen, sulfur, and carbon, respectively.
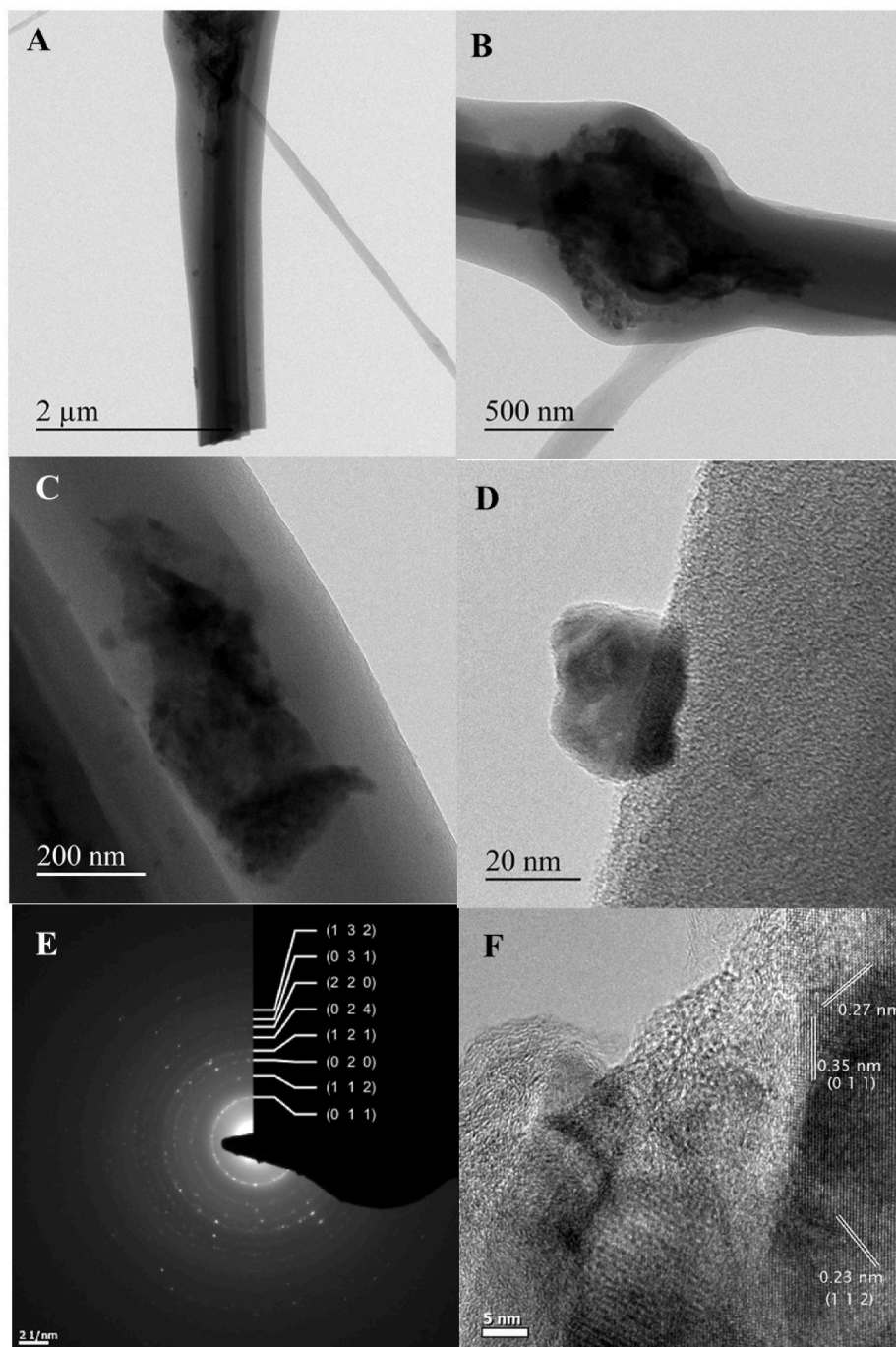
Fig. 3. Transmission electron microscope (TEM) images (A–D) and high-magnification TEM image (B) of TiO_2/C composite fibers prepared from TiS_2/PAN composite fibers, selected area electron diffraction pattern (SAED) pattern (E), and high resolution TEM image (F) of TiO_2/C composite fibers.

and as can be seen in Fig. 1 A, some of the TiS_2 nanoparticles are deposited on the outside and some are suspended within the PAN fibers. The TiS_2 nanoparticles showed a tendency to agglomerate in the precursor polymer solution before centrifugal spinning and the same behavior is observed in the centrifugally spun TiS_2/PAN fibers. Fig. 1 A shows more clearly the agglomerated TiS_2 nanoparticles on the PAN fibers, which is a higher resolution SEM image of the TiS2-PAN fibers. As can be seen in Fig. 1 B, the agglomeration of the particles is exemplified in the nodules formed on the PAN fibers after spinning. After carbonization, the fibers are observed to be shorter, Fig. 1 B. The Ti-based nanoparticles are still shown to be both embedded in and attached to the surface of the carbon-fibers strands. The Ti-based nanoparticles placement inside and side the fibers is exemplified in the high-resolution

SEM image shown in Fig. 1 D. The average diameter observed for the TiS2/PAN fibers before carbonization was determined to be 2.08 ± 0.36 μm, which confirms that centrifugal spinning can produce fibers with larger diameters. After calcination the average diameter of the fibers was determined to be 1.53 ± 0.27 μm, indicating a shrinking in the diameter. The shrinking in diameter is commonly observed in the carbonization of fibers due to the mass loss and conversion of the fibers into amorphous carbon [37].

Fig. 2 shows a dark field STEM image of Ti based C composite fibers and the associated elemental maps for Ti, C, S, and O, respectively. Fig. 2 A focuses on two distinguished fibers after carbonization. As can be seen, the ends of the fibers have a completely different morphology compared to the surface of the fiber, which show the presence of the Titanium
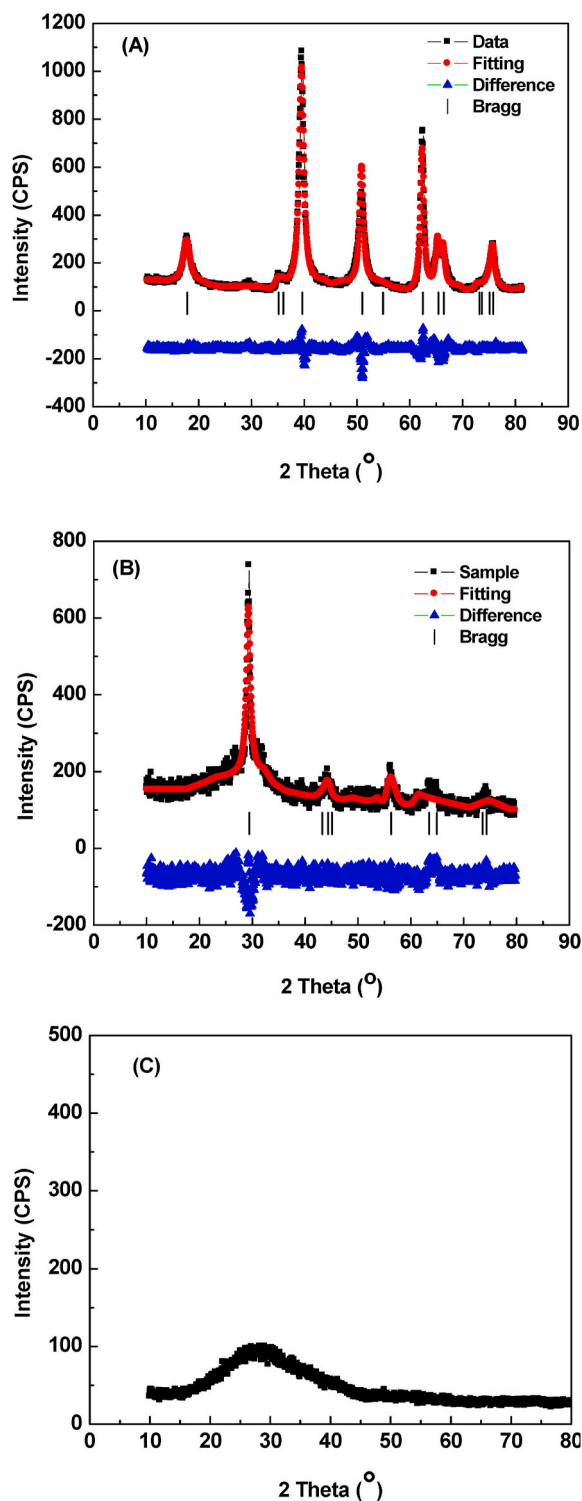
Fig. 4. A) Diffraction pattern of TiS$_2$ nanoparticles with Le Bail fitting. **B)** Diffraction pattern of TiO$_2$/C composite fibers and Le Bail Fitting results. **C)** Diffraction pattern of carbon fibers generated from the carbonization of PAN fibers.

based particles indicated by the arrows. The particles in the top left corner and bottom middle of the two fibers have a diameter between 600 and 800 nm. Fig. 2 B and 2C show the elemental maps of Ti and O the images show a close correlation between the location of the oxygen and titanium atoms within the fibers. The data indicates that more than likely the titanium is bound to oxygen and not sulfur. Fig. 2 D shows

sulfur elemental maps, which do not show correlation between the sulfur and the titanium elemental position indicating that TiS$_2$ is not present in the carbonized fibers. In fact, the sulfur looks homogeneously distributed throughout the fibers, a very low intensity as indicated by the low counts or intensity. The carbon elemental map shows a homogenous distribution of the carbon throughout the fibers as should be observed after carbonization. The elemental distributions can be explained by the conversion of the TiS$_2$ nanoparticles into TiO$_2$ nanoparticles during the calcination of the TiS$_2$/PAN composite fibers in air. As was noted in the EDS maps, the highest concentrations of oxygen (brightest areas in Fig. 2C, indicated by an arrow of O) match closest to the highest concentrations of titanium (brightest areas in Fig. 2 B, indicated by an arrow of Ti). It was also observed that a small feature in the fiber (top left side noted with an arrow) shows only in the oxygen and titanium EDS maps and no high concentration of sulfur was observed.

Fig. 3 shows further analysis of the microstructure of the TiO$_2$/C composite fibers using HRTEM. As can be seen in Fig. 3 (A-D), the contrast between the grey carbon matrix and the black Ti based nanoparticles confirms the formation of Ti based nanoparticles C composite material. It should be noted the Ti based nanoparticles are less than 100 nm and dispersed both inside and outside of the amorphous carbon-fiber matrix as shown in Fig. 3 B. The dispersion of the nanoparticles in the carbon matrix is consistent with the EDS-SEM observation shown in Fig. 2. The TEM analysis confirms that the TiO$_2$ nanoparticles are surrounded by amorphous carbon. In fact, the particles inside the nodules (aggregates or clusters of TiO$_2$ nanoparticles) are surrounded by carbon (Fig. 3 (A-C)). Based on the TEM analysis, the bulk of the nanoparticles are shown to be encapsulated in the carbon; however, evidence of only partial insertion of the nanoparticles in the carbon-fiber matrix was also observed (Fig. 3D).

Fig. 3 E shows the selected area electron diffraction (SAED) pattern of the Ti-based nanoparticles composite fibers. From the SAED pattern, it was determined that the composition of the Ti-based nanoparticles was TiO$_2$ in the anatase phase. The SAED pattern collected from the fibers illustrates several diffraction rings with some regular diffraction high-lighted spots on the rings (Fig. 3 E). The SAED data shows the well-defined polycrystalline nature of the TiO$_2$-nanoparticles. The SAED pattern showed the typical diffraction spots characteristic of the (132), (031), (220), (024), (121), (020), (112) and (011) diffraction planes for the anatase crystal structure of TiO$_2$ [38]. Fig. 3 F shows the higher resolution HRTEM image with the measured d-spacing in the TiO$_2$ nanocrystals. The d-spacing observed in the figure was consistent with the inter-planer spacing for Anatase crystals. The distance between adjacent lattice planes were measured and found to be between 2.3, 2.7, and 3.5 Å which is consistent with the d-spacing observed for anatase (Fig. 3 D).

The TiS$_2$ sample powder XRD pattern was fitted using the Le Bail fitting procedure with fixed intensities of the diffraction lines using the Fullprof 2001 Suite of programs and crystallographic data from the literature [34,38–40].

Fig. 4 A shows the Le Bail fitting of the synthesized TiS$_2$ nanoparticles. The Le Bail fitting confirmed the material synthesized using the solvothermal process was TiS$_2$ in a P3M1 crystal lattice with a = 3.410 Å, b = 3.410 Å, and c = 5.743 Å and α = β = 90 and γ = 120° [34]. The Le Bail fitting procedure ended with a reduced χ^2 of 0.91, indicating a very good agreement between the fitting and the data. The diffraction pattern of the TiS$_2$ nanoparticles suspended in PAN after centrifugal spinning and thermal treatment is shown in Fig. 4 B. A Le Bail fitting of the diffraction pattern was performed from which it was determined that the sample consisted of TiO$_2$ nanoparticles in the anatase phase. The sample had a space group of I4$_1$/amd a = 3.79 Å, b = 3.79 Å, and c = 9.537 Å and α = β = 90° and γ = 90° [38]. In addition, the Le Bail fitting of the anode material had a reduced χ^2 of 1.76 indicating a good agreement between the fitting and the data. Fig. 4C shows the diffraction patterns of the carbonized PAN fibers, which have no diffraction
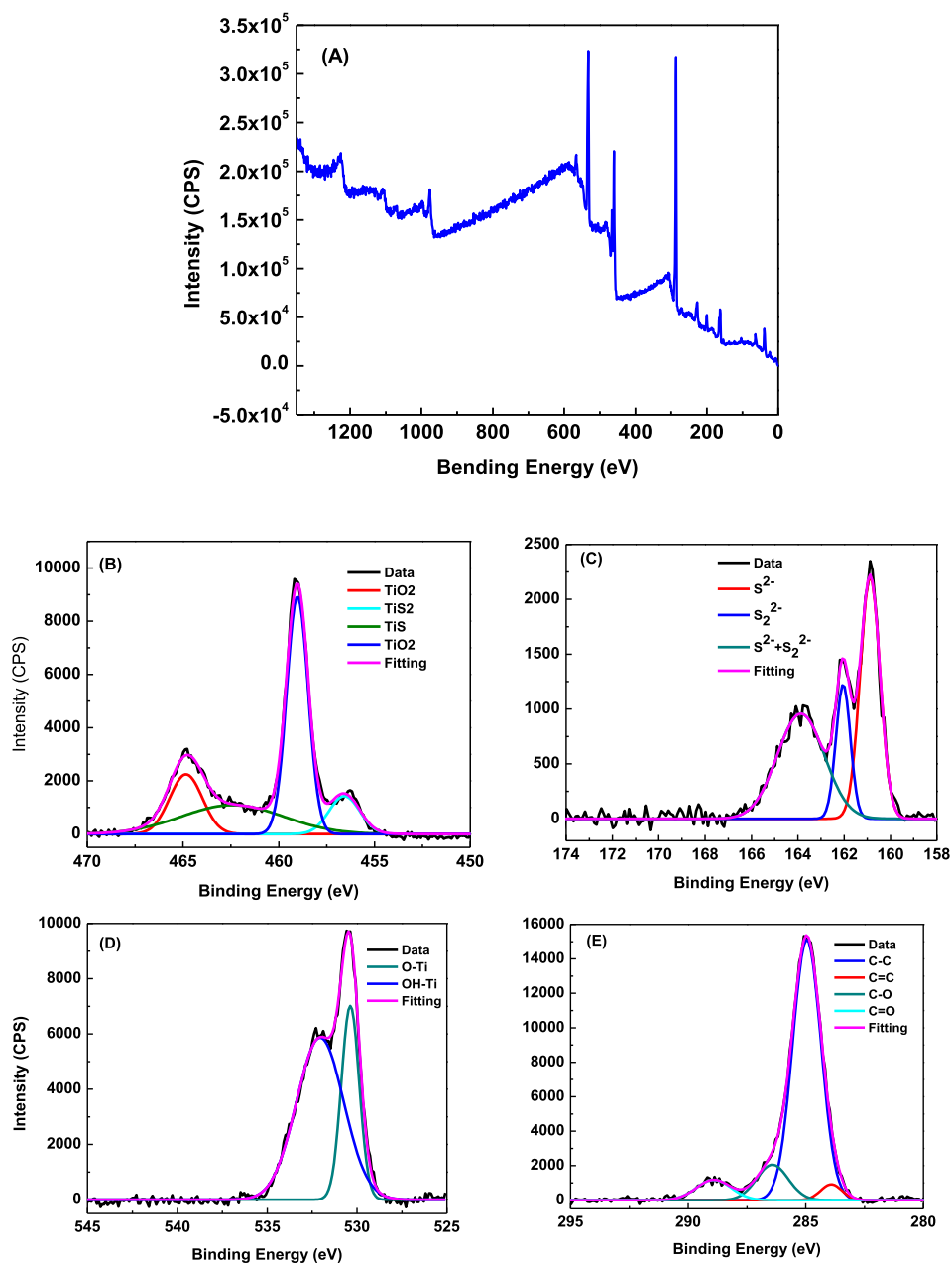
Fig. 5. XPS spectra of synthesized TiS2 nanoparticles (A) survey spectrum and curve fittings of titanium (Ti) (B), sulfur (S) (C), oxygen (O) (D) and carbon (C) (E).

peaks, confirming the amorphous nature of the carbon anode material. The Bragg peaks observed in the fitting for the TiS_2 and the TiO_2 are labeled in each respective materials diffraction pattern. There is a good correlation between determined diffraction planes/families of planes in the SAED in Fig. 3C and the determined planes in TiO_2 in Fig. 4C. The data indicates that the TiS_2 is completely converted to TiO_2 after the carbonization process. The amorphous nature of the TiO_2 phase indicated the production of a low dimensional TiO_2 material. Low dimension layered compounds have shown promising results in the literature as electrode materials in lithium-ion, sodium-ion, and sulfur batteries [11, 41]. Lower dimensional materials and nanomaterials have higher tendency for intercalation and less stress associated with intercalation and de-intercalation. Jing et al. showed that layered TiO_2 in the anatase phase could be synthesized from TiS_2 based nanomaterials [31]. The authors found that the oxidation of the TiS_2 to TiO_2 resulted in single layered TiO_2 due to the reduced van der Waals forces holding the layers of TiS2 together. Jing et al. also showed that single sheets of the anatase

phase were synthesized after lithiation of the TiS_2 and subsequent hydrothermal treatment [31]. Their diffraction pattern of the single layer of TiO_2 is diffused and very similar to that presented in the current manuscript, showing the 101, 112,113,004, 200, 211, and 214/214 diffraction peaks. The conversion of the TiS_2 into TiO_2 would reduce the van der Waals forces and allow the separation of the TiO_2 into individual layers. There is no chemical driving force for the material to maintain the layered TiS_2 structure after oxidation. Also, there is no chemical driving force for the materials to reorganize from the planar structure, which is embedded in the carbon matrix of the anode. To the best of our knowledge, this is the first time to report such results on layered structure of TiO_2/C composite fibers, prepared from TiS_2/PAN fibers, as a binder-free anode for LIBs.

Fig. 5 A shows the XPS survey spectrum data for the TiS_2 nanomaterial a few days after synthesis. As can be seen in Fig. 5 B, the XPS spectrum of the Ti 2P the sample consists of four different curves, which represent two different compounds present in the sample TiS_2 fraction
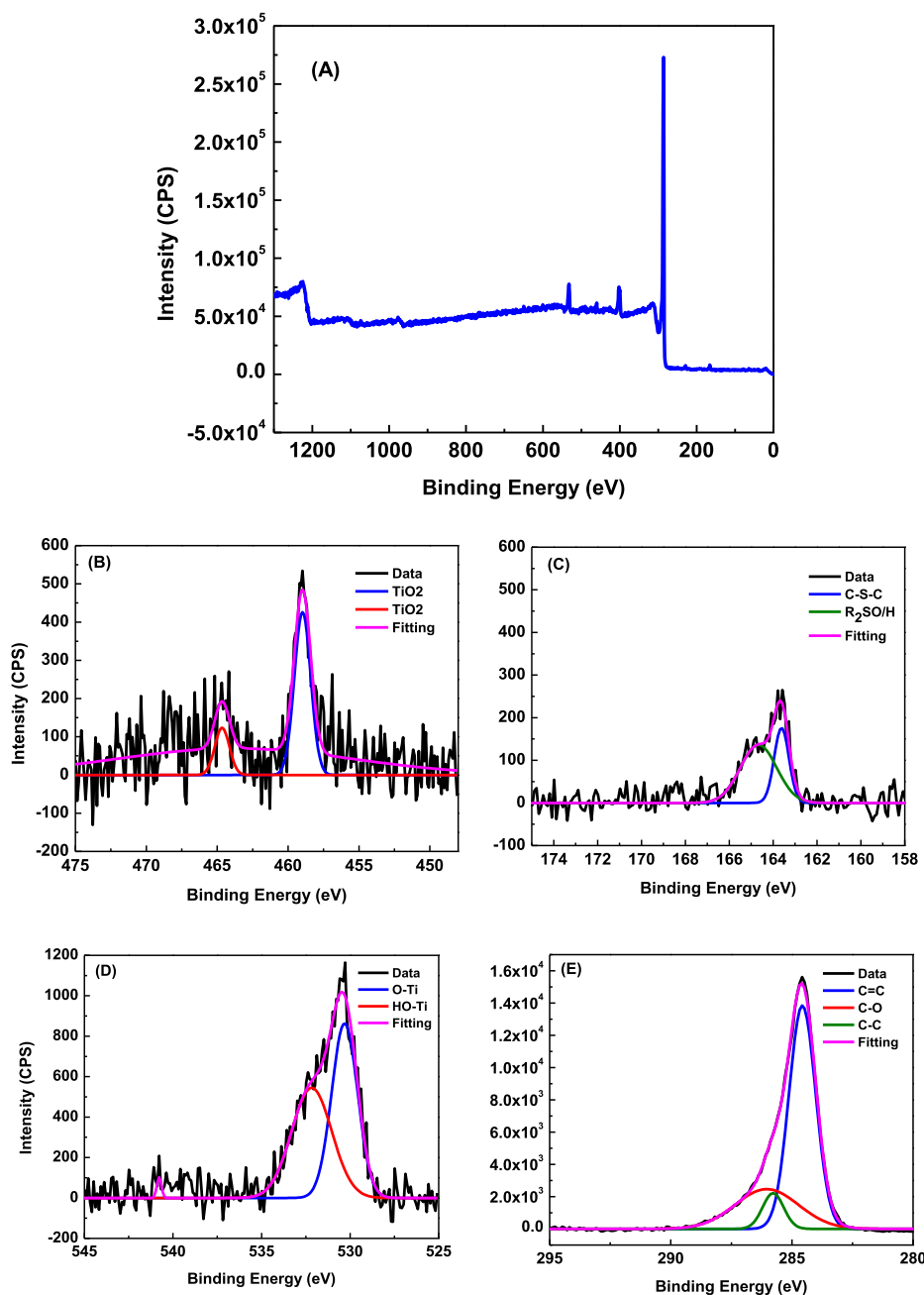
Fig. 6. XPS of synthesized TiS_2 particles/PAN composite fibers after heat treatment. (A) survey spectrum and curve fits of Titanium (Ti) (B), sulfur (S) (C), and oxygen (O) (D), and carbon (C) (E).

and a TiO_2. A similar result was reported by Martinez et al. on the analysis of TiS_2 oxidation from a broken TiS_2 surface [42]. The Ti 2P 456.5 eV and 462.1 eV represent the binding energy for Ti(IV) in TiS_2. Whereas, the peaks observed at 459.0 and 464.7 eV are representative of Ti(IV) in TiO_2 [43]. The Ti 2P XPS data indicate an instability of the TiS_2 nanoparticles when exposed to air causing a surface oxidation, with the high surface area to volume ratio of nanomaterials, and the fact that XPS is a surface technique it makes the amount of TiO_2 present in the sample appear to be higher than the amount of TiS_2 present in the sample. Fig. 5C shows the S 2P XPS spectra of the synthesized TiS_2 nanomaterial. As can be seen from the fitting of the sample, the sample consists of three peaks with binding energies of 160.9, 162.0, and 163.8 eV. The binding energies observed in the S 2P spectra represent the Sulfur present in two states the S^{2-} and S_2^{2-}. The peak observed at 162.0 eV represents a combination of the $S^{2-} + S_2^{2-}$ states [43]. Fig. 5 D shows the XPS

spectrum for the O 1 S spectrum, which shows peaks at 530.4 and 532.0 eV. These peaks are representative of oxygen bound to a metal (Ti–O) bound to metal ions (Ti–OH) [42,44–46]. Some of the oxygen present in the samples is from residual washing compounds and the rest is from the hydrolysis and oxidation of the TiS_2 nanomaterial. Fig. 5 E shows the carbon C 2 S spectrum for the synthesized sample, which consists of 4 peaks, at energies of 284.5, 285.0, 286.5 and 288.9 eV. The binding energies for the C S2P represent carbon present at in the sample C═C, C–C, C–O, and C═O binding environments [47–49]. These are from the solvothermal process used for the synthesis of the nanomaterial and the solvents used for washing the samples. The data indicates there is some residual solvent or washing compounds present after synthesis and washing.

Fig. 6 A shows the XPS survey spectrum for the TiS_2/PAN fibers after the stabilization and carbonization of the precursor fibers. Fig. 6 B shows
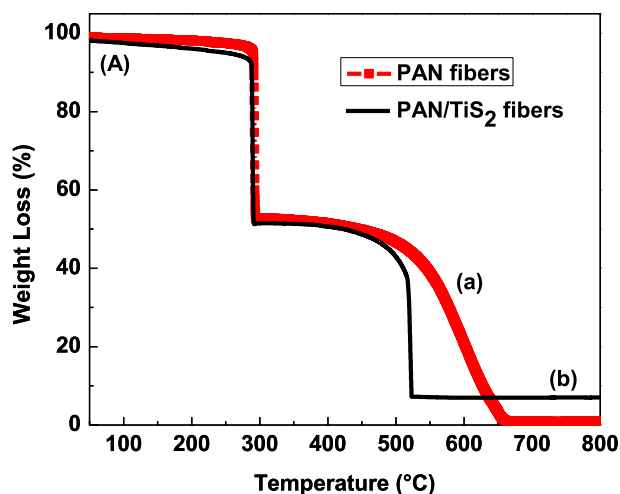
Fig. 7A. TGA thermograms of (a) PAN and (b) TiS$_2$/PAN fibers.

Fig. 7B. DSC thermograms of (a) PAN and (b)TiS2/PAN fibers.

Fig. 8. TGA thermograms of carbon fibers and TiO$_2$/C composite fibers.

the Ti 2P spectrum of the carbonized fibers which consists of two peaks at 459.0 and 464.6 eV, which correspond to Ti bound to oxygen in TiO$_2$ [42]. The data show the complete conversion of the TiS$_2$ to TiO$_2$ after stabilization and carbonization of the TiS$_2$/PAN fibers. Fig. 6C shows the S 2P XPS spectrum of the TiS$_2$ nanoparticles in the carbonized fibers (i.e. TiO$_2$/C fibers). As can be seen in Fig. 6C, the spectrum consists of two peaks located at 163.6 and 164.5 eV, which correspond to sulfur found in the -C-S-C- and in R$_2$-SO/H environments, respectively [50]. This change in the sulfur binding environment is consistent with the observed changes in the Ti 2P XPS results, as well as the SAED and XRD analysis of the samples. Fig. 6 D shows the O 1 S XPS spectrum for the TiS$_2$ nanoparticles in the carbonized fibers. The spectrum was fitted with two different functions with centers located at 530.3 and 532.1 eV, which represent the oxygen bound to a metal and the formation of a metal hydroxide or a metal oxygen carbon bond [42–47]. Fig. 6 E shows the XPS spectrum of carbon in the TiS$_2$/PAN fibers after carbonization and are shown to consist of three different peaks located at 284.5, 285., and 286.0 eV. The three peaks in the fibers are associated with carbon found in the following environments C=C, C–C, and C–O, respectively. The XPS data further confirms the conversion of the TiS$_2$ to TiO$_2$ as was observed in the powder X-ray diffraction analysis.

Fig. 7A shows the TGA thermograms of PAN and TiS$_2$/PAN fibers with 20 wt% TiS$_2$ nanoparticles with respect to PAN in the PAN/DMF precursor solution. The TGA experiments were performed under air atmosphere at a heating rate of 10 °C/min. The PAN and TiS$_2$/PAN fibers show initial weight losses of 3% and 6%, respectively, up to temperatures of 250 °C, which could be due to the loss from adsorbed and bound water. In addition, some of the weight loss may be due to the partial oxidation of the TiS$_2$ nanoparticles. The first major weight loss occurs for the PAN and TiS$_2$/PAN composite-fiber samples at 291 °C and 288 °C, respectively. The transition observed for the PAN fibers at 291 °C is associated with the removal of volatiles and the dehydrogenation, cyclization, as well as crosslinking reactions, which take place within the PAN structure during the stabilization process [51,52]. The mechanism of these reactions depends on the heating rate, medium, weight of the polymer, and type and nature of the filler material [53,54]. The transition observed for the TiS$_2$/PAN fibers at 288 °C is associated with the cyclization reaction in PAN and with the oxidation of the TiS$_2$ nanoparticles in air. The weight loss starting temperature for the PAN fibers is slightly higher than that for the TiS$_2$/PAN fibers, consistent with the DSC results. The PAN fibers exhibited almost 99% weight loss after reaching 670 °C, which was attributed to the oxidation of carbon in air [53]. The thermal stability of the TiS$_2$/PAN fibers was similar to that of the PAN and showed a 7% residue after reaching 525 °C and this amount remained constant up to 800 °C. The TiS$_2$/PAN precursor fibers at the
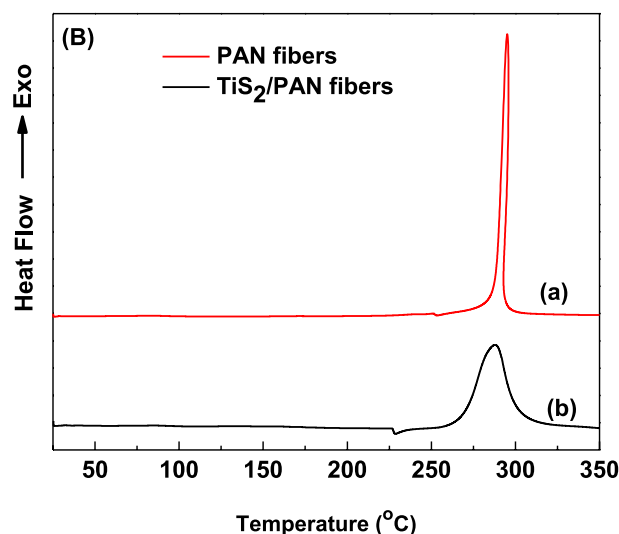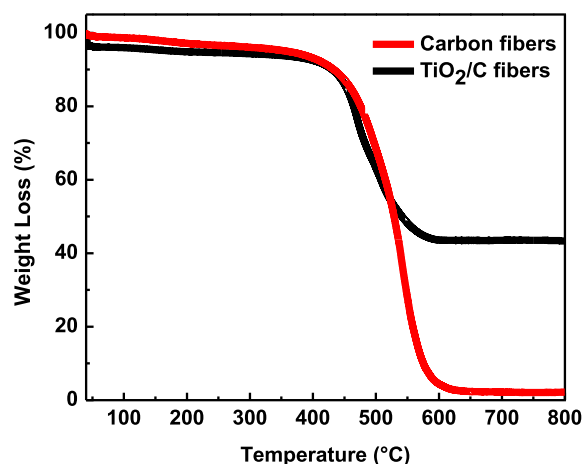
end of the TGA scan contained 7% TiO$_2$ which would indicate an initial amount of TiS$_2$ in the polymer of approximately 10%.

Fig. 7B shows the DSC scans of PAN and PAN/TiS$_2$ precursor fibers under nitrogen. The DSC scans were performed at a heating rate of 5 °C/min. The PAN fibers exhibit a sharp exothermic peak at 295 °C [55] proving that at this temperature several thermal processes were occurred such as cyclization, crosslinking, and dehydrogenation during the heat treatment of PAN precursor fibers. The exothermic peak of the TiS$_2$/PAN precursor fibers shifts slightly to a lower temperature (288 °C) with smaller heat of reaction than that for the PAN fibers. The decreased heat of reaction for the TiS$_2$/PAN precursor fibers is caused by the interactions between TiS$_2$ and PAN which can be attributed to the formation of free radicals of the nitrile groups. A small endothermic peak is observed in the TiS$_2$/PAN fibers at about 226 °C, which may be caused by the trapped solvent in the fibers. A similar endothermic peak was observed for PEO/TiS$_2$ nanocomposites at 180 °C [56].

The amount of carbon in the TiO$_2$/C composite fibers was estimated by conducting TGA experiments on the samples under air environment. The TGA analysis was conducted on TiO$_2$/C composite fibers prepared from TiS$_2$/PAN precursor fibers with 20% weight ratio of TiS$_2$ in the PAN solution. The TGA experiments were performed between 40 and 800 °C at a heating rate of 10 °C/min. TGA analysis was also conducted on carbon fibers prepared from PAN precursor fibers as a control. Fig. 8 shows that the weight loss in the carbon fibers and TiO$_2$/C composite
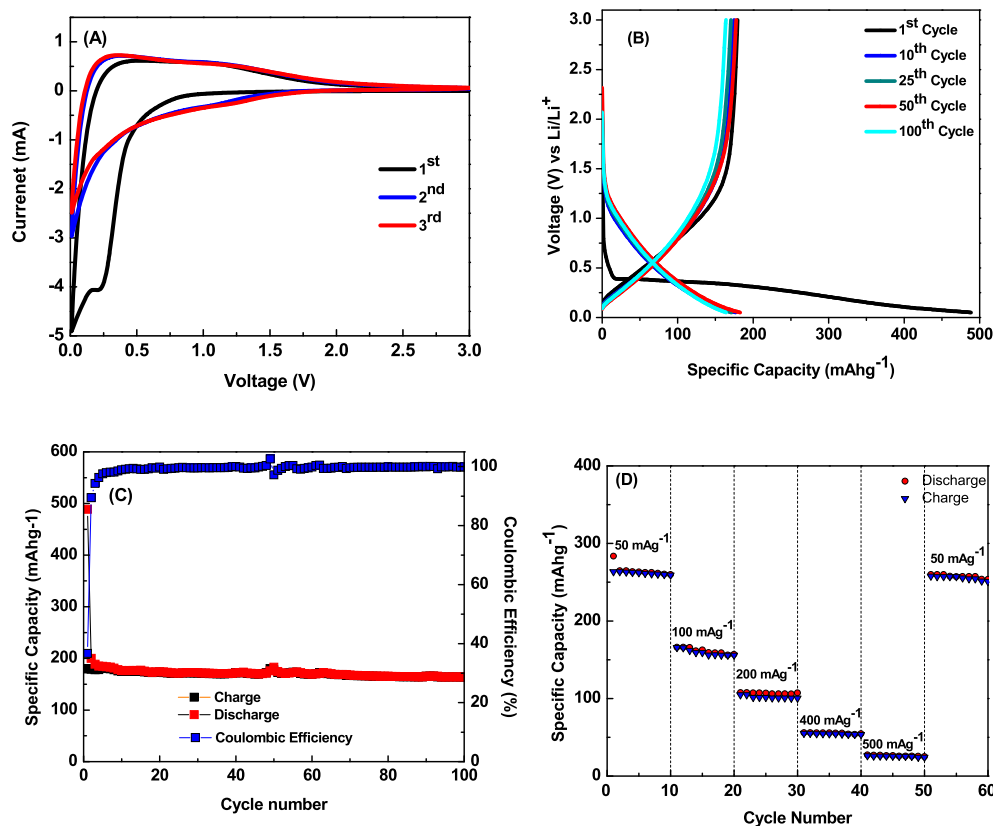
Fig. 9. A) Cyclic voltammetry of carbon-fiber anode in a half cell configuration and cycled between 0.0–3.0V vs. Li/Li$^+$ at low scan rate of 0.2 mV s^{-1}. B) Galvanostatic charge/discharge curves for the carbon-fiber electrode showing the voltage vs specific capacity plots for the 1st, 10th, 25th, 50th and 100th cycles at a current density of 100 mA g^{-1} within a voltage window of 0.05–3.0 V. C) Cycle performance of the carbon fiber electrode at 100 mA g^{-1} between 0.05–3.0 V for 100 cycles. D) rate performance of carbon-fiber electrode at various current densities from 50 mA g^{-1} to 500 mA g^{-1} over 10 cycles.

fibers around 100 °C (about 4%) was due to the evaporation of surface-bound water. Further weight loss is also observed in the CFs and TiO$_2$/C fibers between 100 °C and 200 °C and this is mainly due to the oxidation of the uncarbonized chemical groups in PAN and coordinated water molecules [57]. The carbon fibers and TiO$_2$/C composite fibers show excellent thermal stability up to almost 400 °C. The results show that
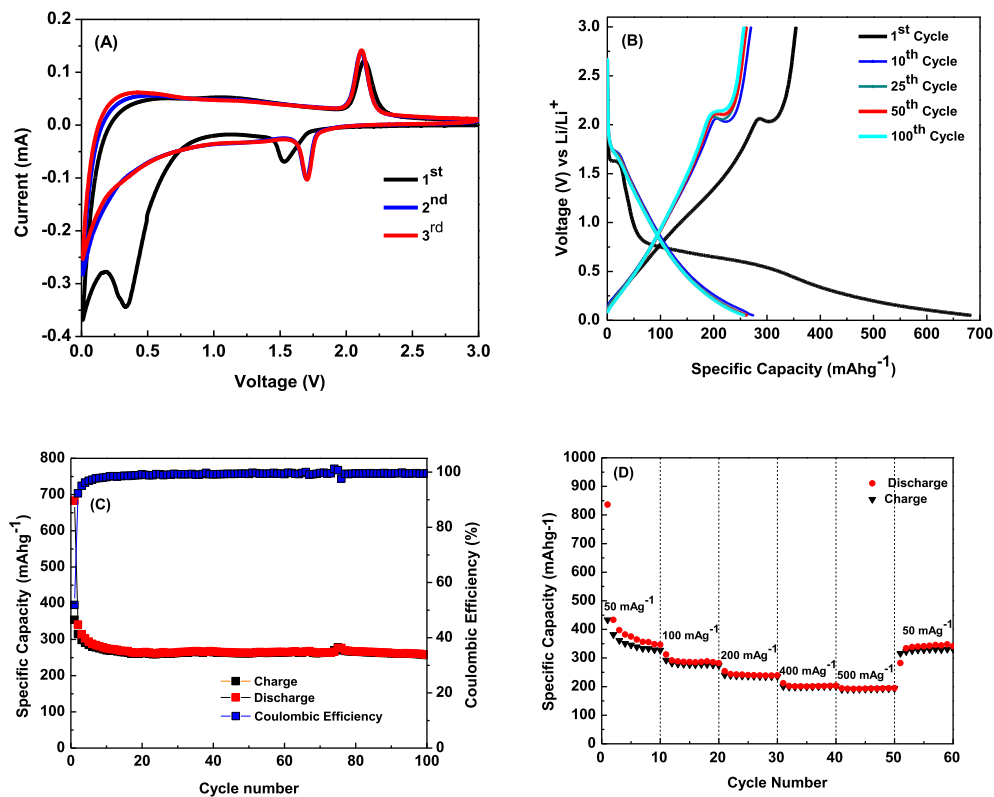

Fig. 10. A) Galvanostatic charge/discharge curves for the TiO$_2$/C composite-fibers electrode showing the voltage vs specific capacity plots for the 1st, 10th, 25th, 50th, and 100th cycles at current density of 100 mA g^{-1} within a voltage window of 0.05–3.0 V. B) Cycle performance of TiO$_2$/C composite electrode at 100 mA g^{-1} for 100 cycles. C) rate performance of TiO$_2$/C composite-fibers electrode at various current densities from 50 mA g^{-1} to 500 mA g^{-1} over 10 cycles. D) Cyclic voltammetry of TiO$_2$/C composite-fibers anode in a half cell configuration and cycled between 0.0 and 3.0 V vs. Li/Li$^+$ at a low scan rate of 0.2 mVs^{-1}.

above 595 °C, 43.5% of the mass is lost and only TiO_2 remains between 700 and 800 °C. However, the residual in the carbonized PAN fibers was 2.75%. This suggests that in TiO_2/C composite fibers, 40.75% TiO_2 was present. Therefore, based on the TGA analysis, the amount of carbon in the TiO_2/C composite fibers is about 59%.

This paragraph and the new figure were included in the revised manuscript.

Fig. 9 A shows the cyclic voltammetry (CV) curves for the unmodified carbon-fiber anode. As can be seen in the figure within the first cathodic scan, a reduction peak at 0.33 V was observed. The reduction peak is associated with the formation of the solid electrolyte interphase (SEI) layer during the first discharge (Li-insertion) cycle [58]. Furthermore, two broad oxidation peaks at located at approximately 0.3 and 1.4 V were also observed. The broad anodic peak at 1.4 V represents lithium-ion extraction from the carbon fibers. The unchanged peaks in the second and third scan demonstrate stability and reversibility of the carbon-fiber anode. To evaluate the electrochemical performance of the carbon-fiber anodes, cycling tests were performed using Li^+ half-cells at a current density of 100 mAg^{-1} over 100 cycles. Fig. 9 B and C depict the intercalation (charge)/de-intercalation (discharge) curves for the carbon-fiber anodes. The galvanostatic charge/discharge experiments were performed over a potential range of 0.01–3 V with a constant current density of 100 mAg^{-1}. At the first discharge cycle (lithium insertion), the carbon fibers showed an initial capacity of 480 mAhg^{-1}. However, the charge capacity (lithium de-insertion) at the first cycle was 180 mAhg^{-1}, indicating a loss of 62% in the first discharge capacity. The large change in capacity can be attributed to the formation of the SEI layer, combined with the high surface-area -to-volume ratio of the carbon fibers. The formation of the SEI has been shown to hinder the electrical contact between the lithium and the carbon-fiber anode [58–60]. The interference in the contact makes the intercalation and de-intercalation processes increasingly difficult, ultimately leading the carbon fibers to show a capacity of 178 mAhg^{-1} after the 100th cycle. Fig. 9C shows the Coulombic efficiency and cycle performance of the carbon fiber-anode over 100 cycles at a current density of 100 mAg^{-1}. The results show a final specific capacity of 178 mAhg^{-1} after 100 cycles. The initial Coulombic efficiency was 37%, which was then maintaining ~99% of that capacity after the 2nd cycle and beyond. Fig. 9 D depicts the rate performance of the carbon-fiber anode, showing delithiation capacities of 260, 160, 110, 70, and 40 mAhg^{-1} at current densities of 50, 100, 200, 400, and 500 mAg^{-1}, respectively. At higher current densities, the high discharge/charge rate during the lithiation (intercalation) and de-intercalation processes results in a low capacity anode, which is caused by the inability of the carbon atoms in the anode to intercalate/de-intercalate with more Li ions. Although the capacity at higher current densities is low, the carbon-fiber anode still recovers to a capacity of 250 mAhg^{-1} at the final current density of 50 mAg^{-1}. The CF-anode shows ~99.8% recovery capability and excellent stability at each of the individual current densities. The data indicate that centrifugally spun carbon fibers can make are good anode materials for LIBs.

Fig. 10 A shows the cyclic voltammetry of TiO_2/C composite fibers in the half-cell configuration and cycled between 0.0 and 3.0 V vs. Li/Li$^+$ at a scan rate of 0.2 mVs^{-1}. On the first cathodic scan, reduction peaks occur at 1.5 V and 0.35 V, while an oxidation peak was observed at 2.1 V during the anodic scan. As previously mentioned, the peak located at 0.35 V is associated with the SEI layer formation. However, the sharp peaks at 1.5 and 2.1 V indicate the reduction of Ti^{4+} to Ti^{3+} during the discharge and subsequent oxidation to Ti^{+4} during the charge cycle, respectively. The CV results show that the peaks for cycles of 2, 3, and 4 are identical, indicating excellent reversibility of TiO_2/C reactions during the charge/discharge cycles [61]. Fig. 10 B shows the charge/discharge curves of the TiO_2/C composite fibers at a constant current density of 100 mAg^{-1}, over a potential range of 0.01–3 V. The first discharge cycle (lithium alloying), the TiO_2/C composite fibers show an initially a high capacity of 683 mAhg^{-1}. However, the initial charge capacities (Li de-insertion) of the TiO_2/C composite anode (lithium
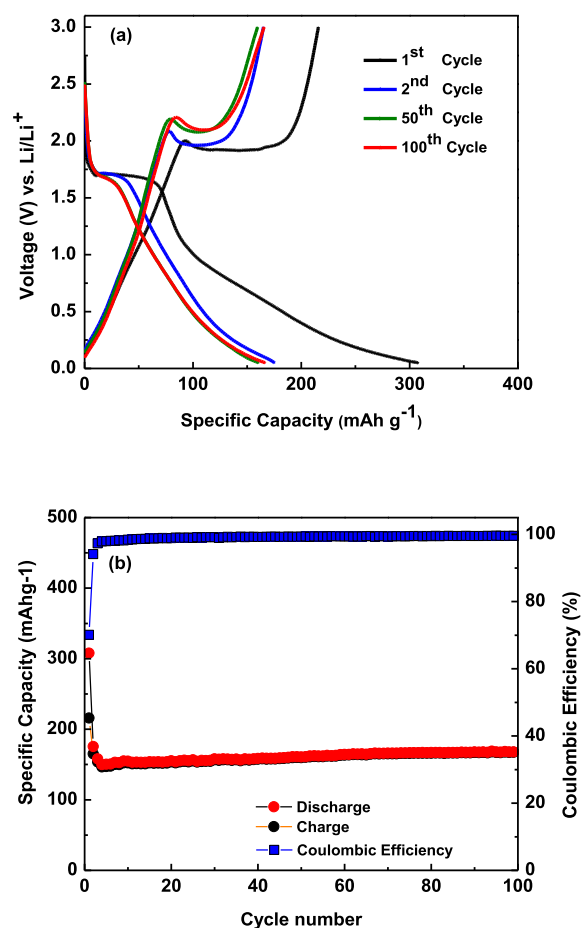
Fig. 11. a) Galvanostatic charge/discharge curves of TiO_2 electrode at 100 mA g^{-1} and b) Cycling performance and coulombic efficiency of TiO_2 electrode.

de-alloying) at 100 mAg^{-1} was observed to be 356 mAhg^{-1}, indicating a loss of 52% in the discharge capacity. The loss in capacity was most likely due to the formation of the SEI layer and the high surface area of the fibers. The interference from the alloying and SEI layer formation makes the alloying and de-alloying of lithium ions during the discharge and charge processes increasingly difficult. Ultimately the interference leads to the TiO_2/C composite fibers to show a 100th cycle capacity of approximately 200 mAhg^{-1} at 100 mAg^{-1}. The initial capacity loss results in the Coulombic efficiency of the Li$^+$ half-cell being ~55%; most of this loss is due to the formation of the SEI layer. Although the initial Coulombic efficiency of the TiO_2/C composite fiber anode is low it is still approximately 10% higher than that observed for the carbon-fiber anode alone. Fig. 10C shows the Coulombic efficiency and cycle performance of the TiO_2/C fiber-anode over 100 cycles at a current density of 100 mAg^{-1}. The results show a final specific capacity of 290 mAhg^{-1} after 100 cycles. The subsequent cycles show excellent stability and a high efficiency of ~99% as can be seen in Fig. 10C, which was similar to that observed for the carbon fiber anodes. Fig. 10 D shows the electrochemical performance of the TiO_2/C composite fibers in terms of capacity versus cycle number at different current densities of 50, 100, 200, 400, and 500 mAg^{-1}, and then again at 50 mAg^{-1}. The TiO_2/C composite fiber anodes exhibit a better rate performance at higher current densities than the carbon fiber anodes. In addition, the TiO_2/C composite fibers demonstrate the ability to recovery after being cycled between high to low current density. The TiO_2/C composite electrode delivered a charge capacity of 300, 253, 198, 200, and 200 mAhg^{-1} at current densities of 50, 100, 200, 400, and 500 mAg^{-1}, respectively. At higher current densities, the discharge/charge rate during the lithiation and delithiation processes of the TiO_2/C composite anode results in a low capacity.
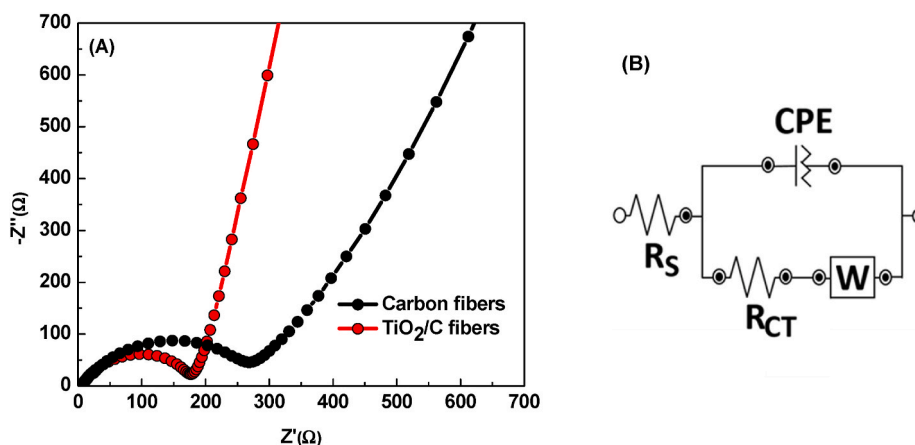
Fig. 12. A) EIS spectra of carbon fiber and TiO$_2$/C composite-fiber electrodes and B) Equivalent circuit model for the EIS results.

Although the capacity at higher current densities was stable at about 200 mAhg^{-1}, the TiO$_2$/C composite anodes still showed a recovery to a capacity of 320 mAhg^{-1} at the final current density of 50 mAg^{-1}. In addition, the TiO$_2$/C composite fibers show ~100% recovery capability and excellent stability at each individual current density. The data show that the TiO$_2$/C composite fibers may be used as anode materials with high power LIBs.

Fig. 11a shows the 1st, 2nd, 50th, and 100th discharge/charge curves for the TiO$_2$ electrode at a current density of 100 mA g^{-1}. The cycling performance and coulombic efficiency of the pure TiO$_2$ electrode at 100 mA g^{-1} are shown in Fig. 11b. It can be observed in Fig. 11a that the first discharge (lithiation) and charge (delithiation) capacities of the TiO$_2$ electrode are 308 and 216, mAh g^{-1}, respectively, resulting in a coulombic efficiency of 70.1%. The TiO$_2$ electrode delivered a reversible charge capacity (lithium-deinsertion) of 165.7 mA h g^{-1} at the 100th cycle indicating a coulombic efficiency of 99.4%. The high irreversible capacity observed for the TiO$_2$ electrode at the first cycle is mainly ascribed to the formation of the SEI layer at the first cycle [58,62].

Electrochemical impedance spectroscopy (EIS) measurements were conducted on Li-ion half cells at an open-circuit voltage to further gain insight into the kinetics and electrochemical performance of the TiO$_2$/C composite-fibers and carbon-fiber electrodes. Fig. 12 A shows Nyquist plots for the carbon-fiber and TiO$_2$/C composite-fiber electrodes. The Nyquist plots for both electrodes show a semicircle at high-medium frequency and an inclined straight line in the low frequency range. The EIS results were further analyzed and fitted with an equivalent circuit shown in Fig. 12 B, where R$_S$ is the electrolyte solution resistance, R$_{CT}$ is the charge transfer resistance, W is the Warburg impedance of Li ion diffusion into the active material, and CPE is the constant phase-angle element equivalent to the double layer capacitance [62]. Based on the fitting procedure of the impedance data, the values for R$_s$ for the carbon fibers and TiO$_2$/C composite fibers were determined to be 6.1 and 5.9 Ω, respectively. The values of the charge transfer resistance, R$_{CT}$, for the carbon fibers and TiO$_2$/C composite fibers were 285 and 180 Ω, respectively. The EIS results show that the electrode reaction kinetics is inversely related to electrochemical impedance. The smaller value of the charge transfer resistance for the TiO$_2$/C composite fibers, compared with the carbon fiber anode, indicate enhanced reaction kinetics and improved electron and ion transport of the TiO$_2$/C composite anode. The decrease in the charge-transfer resistance value of the TiO$_2$/C composite anode resulted in improved rate performance compared to that for the carbon fiber anode. In fact, the impedance results are consistent with the rate performance results for the TiO$_2$/C composite electrode observed in Fig. 10 of the revised manuscript, where the electrode delivered a good performance at a higher current rate compared to that for the carbon-fiber electrode. The present EIS results are in agreement with those reported for carbon fibers and TiO$_2$/C composite fibers electrode

by Jing et al. [63].

4. Conclusion

The solvothermal method utilized in this work was successful for the synthesis of the TiS$_2$ nanoparticles as determined from the diffraction analysis. A nonhomogeneous TiS$_2$-PAN precursor was formed from the centrifugal spinning of the TiS$_2$ nanoparticles in a PAN solution. The thermal treatment of the TiS$_2$/PAN precursor composite-fibers resulted in the generation of TiO$_2$/C composite fibers. The electrochemical experiments showed that the anodes made from TiO$_2$/C composite fibers exhibited good electrochemical performance and excellent rate performance. The TiO$_2$/C composite electrode delivered a high irreversible capacity of almost 200 mAhg^{-1} at a high current rate of 500 mAg^{-1}. The improved electrochemical performance of the TiO$_2$//C composite fibers was attributed to the structure of the TiO$_2$ nanoparticles and their ability to host more Li during alloying/de-alloying processes. Centrifugally spun TiO$_2$/C composite fibers generated from TiS$_2$/PAN precursor fibers may be considered as a potential stable high capacity anode for next generation LIBs for stationary power generation.

Declaration of competing interest

The authors declare that they have no known competing financial interests or personal relationships that could have appeared to influence the work reported in this paper.

References

[1] J.B. Goodenough, K.S. Park, The Li-ion rechargeable battery: a perspective, J. Am. Chem. Soc. 135 (2013) 1167–1176.
[2] J.B. Goodenough, Y. Kim, Challenges for rechargeable Li batteries, Chem. Mater. 22 (2010) 587–603.
[3] V.A. Agubra, L. Zuniga, D. Flores, J. Villareal, M. Alcoutlabi, Composite nanofibers as advanced materials for Li-ion, Li-O-2 and Li-S batteries, Electrochim. Acta 192 (2016) 529–550.
[4] L.W. Ji, Z. Lin, M. Alcoutlabi, X.W. Zhang, Recent developments in nanostructured anode materials for rechargeable lithium-ion batteries, Energy Environ. Sci. 4 (2011) 2682–2699.

[5] S.S. Zhang, Challenges and strategies for fast charge of Li-ion batteries, Chemelectrochem (2020), https://doi.org/10.1002/celc.202000650.

[6] X. Su, Q.L. Wu, J.C. Li, X.C. Xiao, A. Lott, W.Q. Lu, B.W. Sheldon, J. Wu, Silicon-based nanomaterials for lithium-ion batteries: a review, Adv Energy Mater 4 (2014).

[7] Y. Yang, W. Yuan, W.Q. Kang, Y.T. Ye, Y.H. Yuan, Z.Q. Qiu, C. Wang, X.Q. Zhang, Y.Z. Ke, Y. Tang, Silicon-nanoparticle-based composites for advanced lithium-ion battery anodes, Nanoscale 12 (2020) 7461–7484.

[8] H.R. Jung, W.J. Lee, Preparation and characterization of Ni-Sn/carbon nanofibers composite anode for lithium ion battery, J. Electrochem. Soc. 158 (2011) A644–A652.

[9] S. Batool, M. Idrees, J. Kong, J.X. Zhang, S.F. Kong, M.Y. Dong, H. Hou, J.C. Fan, H. G. Wei, Z.H. Guo, Assessment of the electrochemical behaviour of silicon@carbon nanocomposite anode for lithium -ion batteries, J. Alloys Compd. (2020) 832.

[10] D.M. Soares, S. Mukherjee, G. Singh, TMDs beyond MoS2 for electrochemical energy storage, Chem. Eur J. 26 (2020) 6320–6341.

[11] G. Huang, B. Cai, C.F. Zhan, P. Sun, Two-dimensional material as anode for lithium ion batteries: recent progress, Int J Electrochem Sc 15 (2020) 5416–5429.

[12] R.P. Clement, W.B. Davies, K.A. Ford, M.L.H. Green, A.J. Jacobson, Organometallic intercalates of layered transition-metal dichalcogenides Tas2 and Zrs2, Inorg. Chem. 17 (1978) 2754–2758.

[13] L.W. Ji, P. Meduri, V. Agubra, X.C. Xiao, M. Alcoutlabi, Graphene-based nanocomposites for energy storage, Adv Energy Mater 6 (2016).

[14] H.Y. Mou, W. Xiao, C. Miao, R. Li, L.M. Yu, Tin and tin compound materials as anodes in lithium-ion and sodium-ion batteries: a review, Front Chem 8 (2020).

[15] T.F. Zhao, H.B. Shu, Z.H. Shen, H.M. Hu, J. Wang, X.S. Chen, Electrochemical lithiation mechanism of two-dimensional transition-metal dichalcogenide anode materials: intercalation versus conversion reactions, J. Phys. Chem. C 123 (2019) 2139–2146.

[16] Y.F. Qi, J.F. Liu, J.F. Dai, X.Y. Shi, X.J. Zhu, B. Fu, H.Y. Dong, W.G. Zhao, Freestanding SnS carbon composite nanofiber material with excellent electrochemical performance as binder-free negative electrode for lithium-ion batteries, Chemistry 5 (2020) 1792–1796.

[17] H.Y. Wu, X. Chen, C. Qian, H. Yan, C.Y. Yan, N. Xu, Y.Z. Piao, G.W. Diao, M. Chen, Confinement growth of layered WS2 in hollow beaded carbon nanofibers with synergistic anchoring effect to reinforce Li+/Na+ storage performance, Small 16 (2020).

[18] V. Vega-Mayoral, R.Y. Tian, A.G. Kelly, A. Griffin, A. Harvey, M. Borrelli, K. Nisi, C. Backes, J.N. Coleman, Solvent exfoliation stabilizes TiS2 nanosheets against oxidation, facilitating lithium storage applications, Nanoscale 11 (2019) 6206–6216.

[19] L. Zhang, D. Sun, J. Kang, H.T. Wang, S.H. Hsieh, W.F. Pong, H.A. Bechtel, J. Feng, L.W. Wang, E.J. Cairns, J.H. Guo, Tracking the chemical and structural evolution of the TiS2 electrode in the lithium-ion cell using operando X-ray absorption spectroscopy, Nano Lett. 18 (2018) 4506–4515.

[20] S.Y. Chen, Z.X. Wang, X.P. Fang, H.L. Zhao, X.J. Liu, L.Q. Chen, Characterization of TiS2 as an anode material for lithium ion batteries, Acta Phys. Chim. Sin. 27 (2011) 97–102.

[21] B. Kartick, S.K. Srivastava, S. Mahanty, TiS2-MWCNT hybrid as high performance anode in lithium-ion battery, J. Nanoparticle Res. 15 (2013).

[22] M.S. Whittingham, J.A. Panella, formation of stoichiometric titanium disulfide, Mater. Res. Bull. 16 (1981) 37–45.

[23] D.Y. Oh, Y.E. Choi, D.H. Kim, Y.G. Lee, B.S. Kim, J. Park, H. Sohn, Y.S. Jung, All-solid-state lithium-ion batteries with TiS2 nanosheets and sulphide solid electrolytes, J. Mater. Chem. 4 (2016) 10329–10335.

[24] P. Hu, B. Wang, D.D. Xiao, K. Aifantis, Capturing the differences between lithiation and sodiation of nanostructured TiS2 electrodes, Nanomater. Energy 63 (2019).

[25] A. Chaturvedi, E. Edison, N. Arun, P. Hu, C. Kloc, V. Aravindan, S. Madhavi, Two dimensional TiS2 as a promising insertion anode for Na-ion battery, Chemistry 3 (2018) 524–528.

[26] W. Li, K.L. Wang, S.J. Cheng, K. Jiang, An ultrastable presodiated titanium disulfide anode for aqueous "Rocking-Chair" zinc ion battery, Adv Energy Mater 9 (2019).

[27] L. Zuniga, V. Agubra, D. Flores, H. Campos, J. Villareal, M. Alcoutlabi, Multichannel hollow structure for improved electrochemical performance of TiO2/Carbon composite nanofibers as anodes for lithium ion batteries, J. Alloys Compd. 686 (2016) 733–743.

[28] W. Weng, R. Kurihara, J. Wang, S. Shiratori, Electrospun carbon nanofiber-based composites for lithium-ion batteries: structure optimization towards high performance, Compos Commun 15 (2019) 135–148.

[29] K.L. Zhu, X.Y. Liu, J.Y. Du, J.H. Tian, Y. Wang, S.Z. Liu, Z.Q. Shan, In situ synthesis of mesoporous single-grain layer anatase TiO2 nanosheets without additives via a mild and simple process for a long-term Li-ion battery, J. Mater. Chem. 3 (2015) 6455–6463.

[30] S.T. Wang, Y. Yang, Y.H. Dong, Z.T. Zhang, Z.L. Tang, Recent progress in Ti-based nanocomposite anodes for lithium ion batteries, J Adv Ceram 8 (2019) 1–18.

[31] H.K. Jing, Q. Cheng, J.M. Weller, X.S. Chu, Q.H. Wang, C.K. Chan, Synthesis of TiO2 nanosheet photocatalysts from exfoliation of TiS2 and hydrothermal treatment, J. Mater. Res. 33 (2018) 3540–3548.

[32] F.X. Wu, Z.X. Wang, X.H. Li, H.J. Guo, Simple preparation of petal-like TiO2 nanosheets as anode materials for lithium-ion batteries, Ceram. Int. 40 (2014) 16805–16810.

[33] Z.H. Chen, I. Belharouak, Y.K. Sun, K. Amine, Titanium-based anode materials for safe lithium-ion batteries, Adv. Funct. Mater. 23 (2013) 959–969.

[34] S. Prabakar, C.W. Bumby, R.D. Tilley, Liquid-phase synthesis of flower-like and flake-like titanium disulfide nanostructures, Chem. Mater. 21 (2009) 1725–1730.

[35] N. Obregon, V. Agubra, M. Pokhrel, H. Campos, D. Flores, D. De la Garza, Y.B. Mao, J. Macossay, M. Alcoutlabi, Effect of polymer concentration, rotational speed, and solvent mixture on fiber formation using forcespinning((R)), Fibers (2016) 4.

[36] D. Flores, J. Villarreal, J. Lopez, M. Alcoutlabi, Production of carbon fibers through Forcespinning (R) for use as anode materials in sodium ion batteries, Mater Sci Eng B-Adv 236 (2018) 70–75.

[37] Z.Q. Wu, D. Pan, X.B. Fan, B.J. Qian, Thermal shrinkage behavior of preoxidized polyacrylonitrile fibers during carbonization, J. Appl. Polym. Sci. 33 (1987) 2877–2884.

[38] J.H. Leal, Y. Cantu, D.F. Gonzalez, J.G. Parsons, Brookite and anatase nanomaterial polymorphs of TiO2 synthesized from TiCl3, Inorg. Chem. Commun. 84 (2017) 28–32.

[39] J. Rodriguezcarvajal, Recent advances in magnetic-structure determination by neutron powder diffraction, Physica B 192 (1993) 55–69.

[40] A. Le Bail, H. Duroy, J.L. Fourquet, Abinitio structure determination of lisbwo6 by X-ray-powder diffraction, Mater. Res. Bull. 23 (1988) 447–452.

[41] K. Sun, M.S. Fu, Z.H. Xie, D. Su, H. Zhong, J.M. Bai, E. Dooryhee, H. Gan, Improvement of Li-S battery electrochemical performance with 2D TiS2 additive, Electrochim. Acta 292 (2018) 779–788.

[42] H. Martinez, C. Auriel, D. Gonbeau, M. Loudet, G. PfisterGuillouzo, Studies of 1T TIS2 by STM, AFM and XPS: the mechanism of hydrolysis in air, Appl. Surf. Sci. 93 (1996) 231–235.

[43] L.J. Zhu, Q.P. Lu, L.F. Lv, Y. Wang, Y.F. Hu, Z.B. Deng, Z.D. Lou, Y.B. Hou, F. Teng, Ligand-free rutile and anatase TiO2 nanocrystals as electron extraction layers for high performance inverted polymer solar cells, RSC Adv. 7 (2017) 20084–20092.

[44] C.G. Hawkins, L. Whittaker-Brooks, Controlling sulfur vacancies in TiS2-x cathode insertion hosts via the conversion of TiS3 nanobelts for energy-storage applications, Acs Appl Nano Mater 1 (2018) 851–859.

[45] L. Stobinski, B. Lesiak, A. Malolepszy, M. Mazurkiewicz, B. Mierzwa, J. Zemek, P. Jiricek, I. Bielochapka, Graphene oxide and reduced graphene oxide studied by the XRD, TEM and electron spectroscopy methods, J Electron Spectrosc 195 (2014) 145–154.

[46] Y.C.G. Kwan, G.M. Ng, C.H.A. Huan, Identification of functional groups and determination of carboxyl formation temperature in graphene oxide using the XPS O 1s spectrum, Thin Solid Films 590 (2015) 40–48.

[47] Y.M. Xie, P.M.A. Sherwood, X-ray photoelectron spectroscopic studies of carbon-fiber surfaces .11. Differences in the surface-chemistry and bulk structure of different carbon-fibers based on poly(acrylonitrile) and pitch and comparison with various graphite samples, Chem. Mater. 2 (1990) 293–299.

[48] D. Yang, A. Velamakanni, G. Bozoklu, S. Park, M. Stoller, R.D. Piner, S. Stankovich, I. Jung, D.A. Field, C.A. Ventrice, R.S. Ruoff, Chemical analysis of graphene oxide films after heat and chemical treatments by X-ray photoelectron and Micro-Raman spectroscopy, Carbon 47 (2009) 145–152.

[49] P. Stathi, D. Gournis, Y. Deligiannakis, P. Rudolf, Stabilization of phenolic radicals on graphene oxide: an XPS and EPR study, Langmuir 31 (2015) 10508–10516.

[50] K.S. Siow, L. Britcher, S. Kumar, H.J. Griesser, XPS study of sulfur and phosphorus compounds with different oxidation states, Sains Malays. 47 (2018) 1913–1922.

[51] Y. Aykut, B. Pourdeyhimi, S.A. Khan, Effects of surfactants on the microstructures of electrospun polyacrylonitrile nanofibers and their carbonized analogs, J. Appl. Polym. Sci. 130 (2013) 3726–3735.

[52] I.M. Alarifi, W.S. Khan, R. Asmatulu, Synthesis of electrospun polyacrylonitrile-derived carbon fibers and comparison of properties with bulk form, PloS One 13 (2018).

[53] W.S. Khan, M. Ceylan, A. Jabarrania, L. Saeednia, R. Asmatulu, Chemical and thermal investigations of electrospun polyacrylonitrile nanofibers incorporated with various nanoscale inclusions, J. Therm. Eng. 3 (2017) 1374–1389.

[54] W. Dang, J. Liu, X.X. Wang, K.Q. Yan, A.L. Zhang, J. Yang, L. Chen, J.Y. Liang, Structural transformation of polyacrylonitrile (PAN) fibers during rapid thermal pretreatment in nitrogen atmosphere, Polym. Bull. 12 (2020).

[55] L.W. Ji, X.W. Zhang, Fabrication of porous carbon nanofibers and their application as anode materials for rechargeable lithium-ion batteries, Nanotechnology (2009) 20.

[56] J.P. Lemmon, M.M. Lerner, Preparation of nanocomposites of poly(ethylene oxide) with Tis2, Solid State Commun. 94 (1995) 533–537.

[57] C.D.C.W. Cho, Y.- GYunjeh Ko, O.H. Kwon, I.-K. Kang, Stabilization, carbonization, and characterization of PAN precursor webs processed by electrospinning technique, Carbon letters 8 (2007) 313–320.

[58] Z. Hou, J.L. Zhang, W.H. Wang, Q.W. Chen, B.H. Li, C.L. Li, Towards high-performance lithium metal anodes via the modification of solid electrolyte interphases, J Energy Chem 45 (2020) 7–17.

[59] S.J. An, J.L. Li, C. Daniel, D. Mohanty, S. Nagpure, D.L. Wood, The state of understanding of the lithium-ion-battery graphite solid electrolyte interphase (SEI) and its relationship to formation cycling, Carbon 105 (2016) 52–76.

[60] Y.X. Lin, Z. Liu, K. Leung, L.Q. Chen, P. Lu, Y. Qi, Connecting the irreversible capacity loss in Li-ion batteries with the electronic insulating properties of solid electrolyte interphase (SEI) components, J. Power Sources 309 (2016) 221–230.

[61] S.S. El-Deen, A.M. Hashem, A.E. Abdel Ghany, S. Indris, H. Ehrenberg, A. Mauger, C.M. Julien, Anatase TiO2 nanoparticles for lithium-ion batteries, Ionics 24 (2018) 2925–2934.

[62] Y.Q. Fu, Q.L. Wei, X.Y. Wang, H.B. Shu, X.K. Yang, S.H. Sun, Porous hollow alpha-Fe2O3@TiO2 core-shell nanospheres for superior lithium/sodium storage capability, J. Mater. Chem. 3 (2015) 13807–13818.

[63] M.X. Jing, J.Q. Li, C. Han, S.S. Yao, J. Zhang, H.A. Zhai, L.L. Chen, X.Q. Shen, K. S. Xiao, Electrospinning preparation of oxygen-deficient nano TiO2-x/carbon fibre membrane as a self-standing high performance anode for Li-ion batteries, Roy Soc Open Sci 4 (2017).